The energetics of large-scale internal wave degeneration in lakes

By L. BOEGMAN, G. N. IVEY and J. IMBERGER

Centre for Water Research, The University of Western Australia, Crawley, WA 6009 Australia

Field observations in lakes, where the effects of the Earth's rotation can be neglected, suggest that the basin-scale internal wave field may be decomposed into a standing seiche, a progressive nonlinear surge and a dispersive solitary wave packet. In this study we use laboratory experiments to quantify the temporal energy distribution and flux between these three component internal wave modes. The system is subjected to a single forcing event creating available potential energy at time zero (APE). During the first horizontal mode one basin-scale wave period (T_i), as much as 10 % and 20 % of the APE may be found in the solitary waves and surge, respectively. The remainder is contained in the horizontal mode one seiche or lost to viscous dissipation. These findings suggest that linear analytical solutions, which consider only basin-scale wave motions, may significantly underestimate the total energy contained in the internal wave field. Furthermore, linear theories prohibit the development of the progressive nonlinear surge, which serves as a vital link between basin-scale and sub-basin-scale motions. The surge receives up to 20 % of the APE during a nonlinear steepening phase and, in turn, conveys this energy to the smaller-scale solitary waves as dispersion becomes significant. This temporal energy flux may be quantified in terms of the ratio of the linear and nonlinear terms in the nonlinear non-dispersive wave equation. Through estimation of the viscous energy loss, it was established that all inter-modal energy flux occurred before $2T_i$; the modes being independently damped thereafter. The solitary wave energy remained available to propagate to the basin perimeter, where although it is beyond the scope of this study, wave breaking is expected. These results suggest that a periodically forced system with sloping topography, such as a typical lake, may sustain a quasi-steady flux of 20 % of APE to the benthic boundary layer at the depth of the metalimnion.

1. Introduction

Internal waves were first observed in lakes by Watson (1904) and Wedderburn (1907). They interpreted a temperature oscillation in Loch Ness as a wind-driven uninodal baroclinic *standing seiche*. Subsequent investigations by Mortimer (1955) and Thorpe (1971) revealed a progressive component to the Loch's basin-scale internal wave field. This wave was asymmetrical in character, owing to a steep 'nonlinear' wave front and is typically referred to as a *progressive internal surge*. Remarkably similar observations from other lakes abound (e.g. Hunkins & Fliegel 1973; Farmer 1978; Mortimer & Horn 1982; Boegman *et al.* 2003). These observations show the internal surge to contain a packet of spatially coherent large-amplitude *internal solitary waves* which are followed by an oscillatory tail of irregular wavelength. The high-frequency solitary waves are expected to break upon sloping topography at the basin perimeter

leading to enhanced dissipation, fluxes and bioproductivity (e.g. Ostrovsky *et al.* 1996; MacIntyre *et al.* 1999; Michallet & Ivey 1999; Kunze *et al.* 2002). Laboratory studies suggest that between 5 % and 25 % (Helfrich 1992; Michallet & Ivey 1999) of the incident solitary wave energy may be converted by diapycnal mixing to an irreversible increase in the potential energy of the water column. However, the evolution, propagation and breaking of internal solitary waves are not reproduced in field scale hydrodynamic and water quality models (e.g. Hodges *et al.* 2000; Boegman *et al.* 2001). This is a consequence of the waves being dispersive, resulting from non-hydrostatic proceesses, and having wavelengths of order 100 m (Boegman *et al.* 2003), much smaller than the feasible grid-point spacing. At present, these effects may not be parameterized because the distribution and flux of energy between the standing waves, the internal surge and the solitary waves remains unknown (Imberger 1998; Horn, Imberger & Ivey 2001).

In this study we address these issues by using a laboratory model to quantify the temporal energy distribution between the component internal wave modes: the baroclinic standing seiche, the progressive internal surge and the internal solitary waves. We seek to cast our results in terms of parameters that are external to the evolving sub-basin-scale flow (e.g. wind speed, quiescent pycnocline depth, etc.). This will facilitate engineering application and parameterization into field-scale hydrodynamic models. We consider systems in which the effects of the Earth's rotation can be neglected and that are subject to a single forcing event. In §2, we present the relevant theoretical background. The laboratory experiments are described in §3, followed by a presentation of results and a comparison to an analytical model. Finally, in §4 we estimate the loss of energy to the action of viscosity and are thus able to evaluate the modal energy flux. In conclusion, our results are placed within the context of what is presently known about the energetics of stratified lakes.

2. Theoretical background

During the summer months, a stratified lake will typically possess a layered structure consisting of an epilimnion, a metalimnion and a hypolimnion. If the vertical density gradient is abrupt through the metalimnion, the lake may be approximated as a simple two-layer system of depth h_1 and density ρ_1 over depth h_2 and density ρ_2, where $H = h_1 + h_2$ is the total depth and L denotes the basin length (e.g. Heaps & Ramsbottom 1966; Thorpe 1971; Farmer 1978). Internal waves may be initiated within a stratified lake by an external disturbance such as a surface wind stress. The internal response of the waterbody to a wind stress, as described by Fischer *et al.* (1979) and Spigel & Imberger (1980), can be gauged by the ratio of the wind disturbance force to the baroclinic restoring force. Thompson & Imberger (1980) introduced this ratio as the Wedderburn number W, which may be expressed for our two-layer system (see, Horn *et al.* 2001) as

$$W^{-1} = \frac{\eta_o}{h_1}, \tag{2.1}$$

where η_o is the amplitude of the initial disturbance. Note that when $W \approx 1$ the thermocline has upwelled to the surface at the windward shore.

From the initial condition of a tilted thermocline, Horn *et al.* (2001) applied two-layered theoretical descriptions, verified by laboratory experiments, to identify the mechanisms responsible for the degeneration of the evolving large-scale interfacial gravity wave field. Through comparison of the characteristic time scales of the various degeneration mechanisms, they defined five regimes in which a particular mechanism
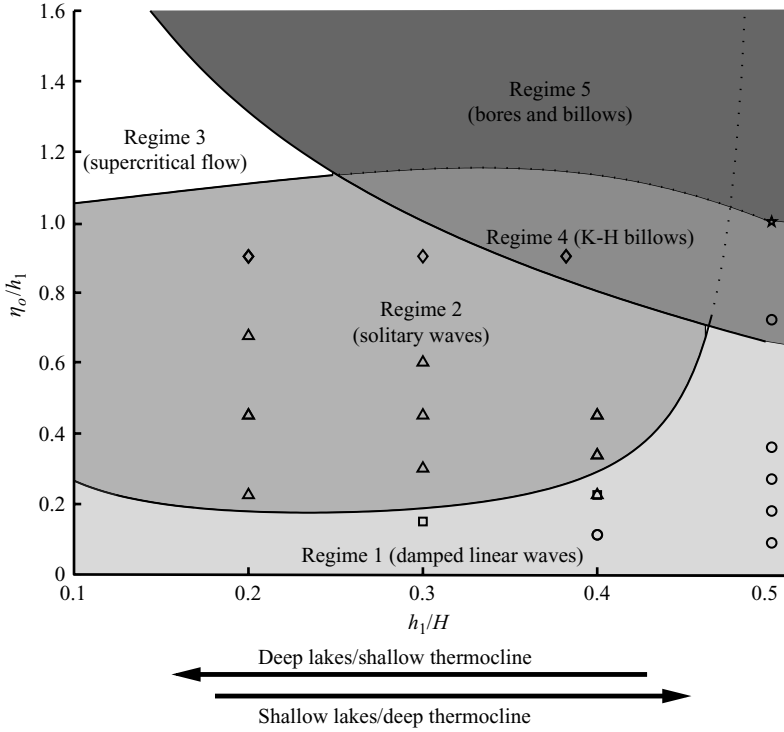
FIGURE 1. Analytical regime diagram characterizing the degeneration of large-scale gravity waves, plotted in terms of the normalized initial forcing scale η_o/h_1 and the depth ratio h_1/H. The laboratory observations are also plotted ($\star$, Kelvin–Helmholtz (K-H) billows and bore; $\diamond$, broken undular bore; $\triangle$, solitary waves; $\square$, steepening; $\circ$, damped linear waves). Reproduced from Horn *et al.* (2001).

was expected to dominate (figure 1). For small to medium-sized lakes subject to weak forcing ($W^{-1} < 0.3$) an internal standing seiche is generated that is eventually damped by viscosity. Moderate forcing ($0.3 < W^{-1} < 1$), results in the production of a progressive internal surge and internal solitary waves.

For weak initial disturbances ($W^{-1} < 0.3$), the standing internal seiche that forms is well described by the linear non-dispersive wave equation (e.g. Gill 1982, p. 127),

$$\frac{\partial^2 \eta}{\partial t^2} = c_o^2 \frac{\partial^2 \eta}{\partial x^2}, \qquad (2.2)$$

where $\eta(x, t)$ (positive upward) is the interfacial displacement, $c_o = \sqrt{(g'h_1 h_2)/(h_1 + h_2)}$ the linear long-wave speed and $g' = g(\rho_2 - \rho_1)/\rho_2$ the reduced gravity at the interface. Equation (2.2) admits periodic sinusoidal solutions of the form (e.g. Mortimer 1974)

$$\eta = a \cos(kx + \omega t), \qquad (2.3)$$

where a is the wave amplitude, ω the wave frequency, $k = 2\pi/\lambda$ the wavenumber and $\lambda = 2L$ the fundamental wavelength. The period of an internal seiche $T_i = 2\pi/\omega$ for an enclosed basin is

$$T_i^{(n)} = \frac{2L}{nc_o}, \qquad (2.4)$$

where $n = 1, 2, 3$, etc. denotes the horizontal mode. Hereinafter, the fundamental time scale T_i, without superscript, will be used to represent the gravest mode where $n = 1$.

A particular solution to (2.2) may be obtained for a rectangular tank stratified with two superposed incompressible fluids of differing density. The no-flux boundary conditions at the endwalls require the horizontal velocity to vanish and the fluid interface to remain perpendicular to the boundary, such that

$$\frac{\partial \eta}{\partial x}(0, t) = \frac{\partial \eta}{\partial x}(L, t) = 0, \tag{2.5}$$

for $t > 0$. The initial conditions consist of a tilted interface with maximum displacement denoted by η_o and no initial motion

$$\eta(x, 0) = \frac{2\eta_o}{L}x - \eta_o, \qquad \frac{\partial \eta}{\partial t}(x, 0) = 0, \tag{2.6}$$

for $0 \leqslant x \leqslant L$. The available potential energy of the perturbed state at $t = 0$ is given by integration of the general equation for the available potential energy (APE) (e.g. Cushman-Roisin 1994, p. 213)

$$\text{APE} = \frac{g(\rho_2 - \rho_1)}{2} \int_0^L \eta^2(x, t)\, dx, \tag{2.7}$$

over the initial condition, leading to

$$\text{APE}_{t=0} = \tfrac{1}{6}gL(\rho_2 - \rho_1)\eta_o^2. \tag{2.8}$$

The general solution is

$$\eta(x, t) = \sum_{n=1}^{\infty} k_n \cos\left(\frac{n\pi}{l}x\right) \cos\left(\frac{c_o n\pi}{l}t\right), \tag{2.9}$$

where k_n are the coefficients in the Fourier cosine series

$$k_n = \frac{2}{L} \int_0^L \left(\frac{2\eta_o}{L}x - \eta_o\right) \cos\left(\frac{n\pi}{L}x\right) dx \qquad (n = 1, 3, 5\ldots) \tag{2.10}$$

$$= \frac{-8\eta_o}{(n\pi)^2}. \tag{2.11}$$

Figure 2(a–i) shows the evolution of the initial condition consisting of component waves progressing from the boundaries (denoted by arrows). The resultant standing wave pattern and associated baroclinic flow is periodic for each mode n, the period given by (2.4). At $t = 0$, all wave energy is distributed in the potential form between the odd modes (figure 2j–o). The modal distribution of available potential energy resulting from the initial condition is given by substituting (2.9) and (2.10) into the general equation for the available potential energy (2.7), resulting in

$$\text{APE}^{(n)} = 16\frac{gL(\rho_2 - \rho_1)\eta_o^2}{(n\pi)^4} \qquad (n = 1, 3, 5\ldots) \tag{2.12}$$

which may be summed over n where

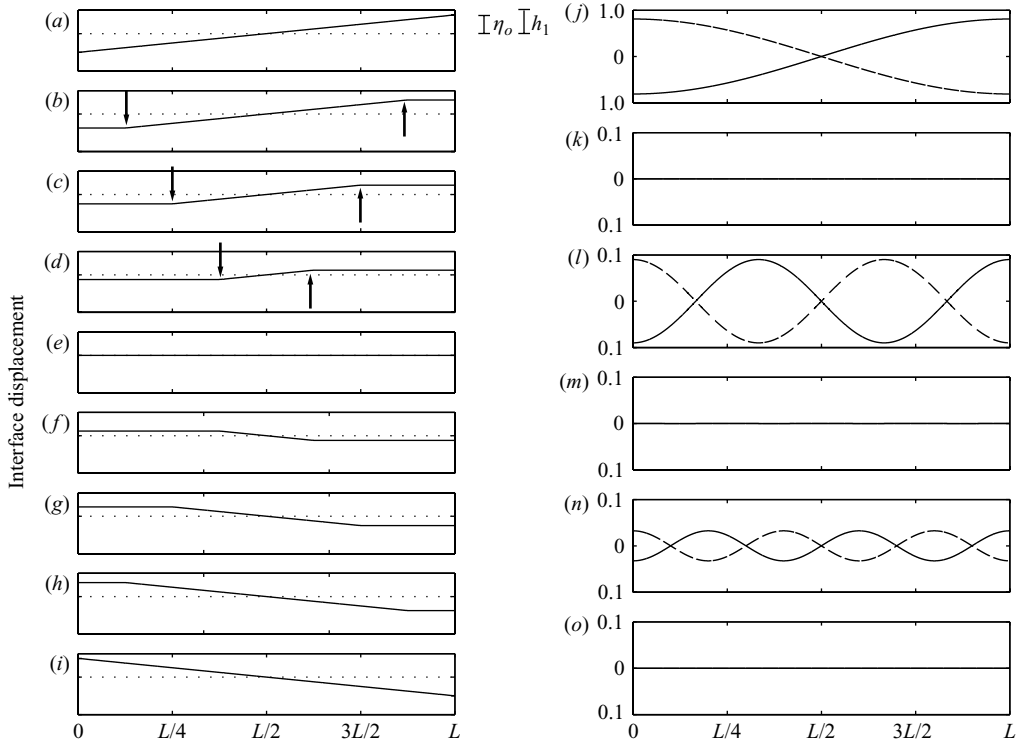$$\sum_{n=0}^{\infty} \frac{16}{[(2n+1)\pi]^4} = \tfrac{1}{6}, \tag{2.13}$$

FIGURE 2. Solution of the wave equation initial-value problem resulting from a tilted interface. (*a*–*i*) Evolution of the interface position. Panels are shown over half an internal wave period ($0 < t < T_i/2$) at intervals of $T_i/16$. The flow reverses (i.e. (*i*–*a*)) over $T_i/2 < t < T_i$. (*j*–*o*) Interfacial displacement of horizontal modes $n = 1$ to 6, respectively, at $t = 0$ (solid line) and $t = T_i/2$ (broken line). For description of arrows see text.

to give (2.8). This equality between the APE in the initial condition (from (2.6)) and the sum of the APE calculated independently for the horizontal modes (from (2.9) at $t = 0$) demonstrates that the modes given by (2.9) are a complete set.

Comparison of (2.8) and (2.12) reveals that the energy is partitioned between the odd modes with 98.6 %, 1.2 % and 0.2 % of the initial energy in $APE_{n=1}$, $APE_{n=3}$ and $APE_{n=5}$, respectively. For a non-dissipative system, these modal energy distributions represent the sum of kinetic and potential energy and are independent of time.

For moderate initial disturbances ($0.3 < W^{-1} < 1$), nonlinearities become significant and an additional term is required in the governing wave equation. For illustrative simplicity, we consider progressive unidirectional motions described by the nonlinear and non-dispersive wave equation

$$\frac{\partial \eta}{\partial t} + c_o \frac{\partial \eta}{\partial x} + \alpha \eta \frac{\partial \eta}{\partial x} = 0, \qquad (2.14)$$

where the nonlinear coefficient $\alpha = (3c_o/2)(h_1 - h_2)/h_1 h_2$ (see, for example, Djordjevic & Redekopp 1978; Kakutani & Yamasaki 1978). Bi-directional propagation and/or endwall reflection would require a Boussinesq type equation (e.g. New & Pingree 2000; Redekopp 2000; Horn *et al.* 2002). The dependence of α on $(h_1 - h_2)$ suggests that the degree of nonlinearity in the system depends on the relative heights of the stratifying layers as well as the local interfacial displacement $\eta(x, t)$.

Nonlinear waves will steepen under a balance between the unsteady ($\partial\eta/\partial t$) and nonlinear $\alpha\eta(\partial\eta/\partial x)$ terms (Long 1972; Horn, Imberger & Ivey 1999). This leads to a steepening timescale T_s (Horn *et al.* 2001)

$$T_s = \frac{L}{\alpha\eta_o}. \tag{2.15}$$

As a wave steepens, dispersive effects become significant, eventually balancing non-linear steepening (Hammack & Segur 1978). This results in the formation of higher-frequency waves of permanent form. These waves often occur in lakes and oceans as localized single entities and are thus called 'solitary waves'. Internal solitary waves may be modelled to first order in amplitude using the weakly nonlinear Kortweg–de Vries (KdV) equation (e.g. Benney 1966; Gear & Grimshaw 1983; Horn *et al.* 2002)

$$\frac{\partial\eta}{\partial t} + c_o\frac{\partial\eta}{\partial x} + \alpha\eta\frac{\partial\eta}{\partial x} + \beta\frac{\partial^3\eta}{\partial x^3} = 0, \tag{2.16}$$

where the dispersive coefficient $\beta = c_o h_1 h_2/6$. Note that if the interface occurs at mid-depth, α vanishes thus inhibiting steepening and the subsequent production of solitary waves. A particular solution to (2.16) is the solitary wave (Benney 1966)

$$\eta(x - ct) = a\,\text{sech}^2\left(\frac{x - ct}{\lambda}\right), \tag{2.17}$$

where the phase velocity c and horizontal length scale are given by

$$c = c_o + \tfrac{1}{3}\alpha a, \qquad \lambda^2 = 12\frac{\beta}{a\alpha}. \tag{2.18}$$

An estimate of the number and amplitude of solitary waves, while beyond the scope of this study, may be obtained from the Schrödinger equation based on inverse scattering theory (e.g. Landau & Lifshitz 1959; Whitham 1974; Apel *et al.* 1985; Drazin & Johnson 1989; Horn *et al.* 1999).

In general, the internal field that can evolve from the set-up or relaxation of the thermocline is a combination of linear standing seiches, nonlinear progressive surges and dispersive solitary waves. Each process occurring over differing time scales (Horn *et al.* 2001). These motions have been qualitatively reproduced for a two-layer stratification in a rectangular box, both experimentally (Thorpe 1971, 1974) and analytically (Horn *et al.* 2002). In general, the nonlinear and non-hydrostatic nature of the problem does allow derivation of the interfacial displacements resulting from the linear, nonlinear and non-hydrostatic internal wave modes (e.g. Peregrine 1966; Mortimer 1974; Horn *et al.* 1999; Miller & Clarke 2001); however, the distribution and flux of energy between these coupled modes has remained analytically untractable (Redekopp 2000). We address this issue in the following sections through the use of laboratory experiments to quantify both the temporal energy distributions and the fluxes.

3. Laboratory experiments

3.1. *Experimental methods*

Experiments were conducted in a sealed rectangular acrylic tank 6 m long, 0.3 m wide and 0.29 m deep (figure 3a). The data were originally collected for the study by Horn *et al.* (2001). The tank was filled with a two-layer stratification by tilting the tank about its central axis (to a maximum angle of 23° from horizontal) and partially filling the tank with the volume of water required for the upper fresh-water layer. From a
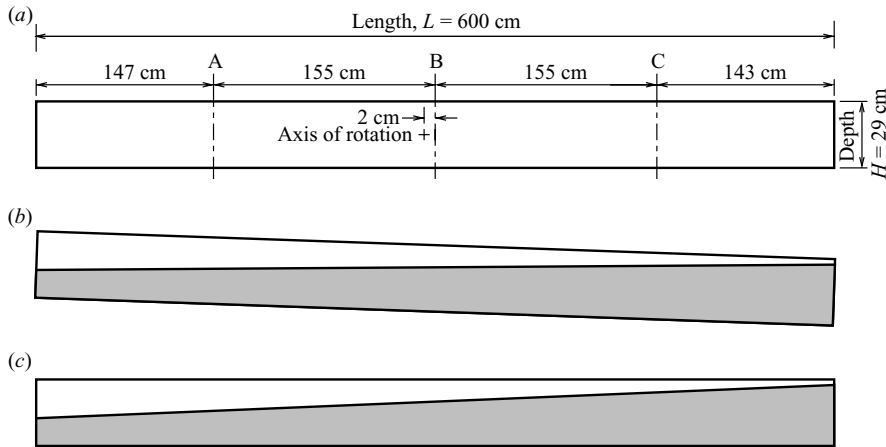
FIGURE 3. (*a*) Schematic diagram of the experimental set-up. The ultrasonic wave gauges were located at the positions marked A, B and C. (*b*) Initially tilted tank. (*c*) Initial condition with the tank horizontal and the interface inclined. Reproduced from Horn *et al.* (2001).

reservoir of saline water, the lower layer was slowly pumped into the bottom of the tank, thus displacing the buoyant fresh-water layer. Once full, the tank was gradually rotated to a horizontal position resulting in a stretching of the isopycnal surface and an increase in the density gradient within the interface. For visualization purposes, the interface or one of the two layers was seeded with dye. Prior to commencing an experiment the tank was rotated to the required interfacial displacement angle (figure 3*b*). From this condition, the set-up and subsequent relaxation from a wind stress was simulated through a rapid rotation of the tank to the horizontal position, leaving the interface inclined at the original angle of tilt of the tank (figure 3*c*). Each time the tank was filled with a particular stratification, a set of experiments were carried out with increasing angles of tilt. This resulted in a gradual thickening of the density interface over the course of experiments, from about 1 to 2 cm. The resulting vertical displacements of the density interface $\eta(x, t)$ were measured using three ultrasonic wave gauges (Michallet & Barthélemy 1997) distributed longitudinally along the tank at locations A, B and C. (figure 3*a*). The wave gauges logged data to a personal computer at 50 Hz via a 12-bit analogue-to-digital converter. The experimental variables considered in this study, together with the resolution with which they were determined are given in table 1.

3.2. *Experimental observations*

At the beginning of each experiment the flow was driven by the baroclinic pressure gradient that resulted from the tilted density interface (figure 4*a*). The fluid layers were observed to accelerate rapidly from rest, the lower layer moving toward the downwelled end of the tank and a corresponding return flow in the upper layer. This motion was characteristic of a standing horizontal mode one (H1) seiche (figure 4*a*–*f*). The progressive surge (figure 4*c*–*d*) and solitary waves (figure 4*e*–*i*) were also clearly visible, causing the observed internal wave field to deviate significantly from the linear model (figure 2*a*–*i*). The progressive surge and solitary wave packet may be qualitatively compared to an undular hydraulic jump (e.g. Henderson 1966, his figure 6–29a), where the frame of reference is vertically inverted to match the corresponding relative thicknesses of the superposed fluid layers. However, the internal surge

Run	h_1/H	θ (deg.)	$W^{-1} = (\eta_o/h_1)$	T_s (s)
1	0.20	0.34	0.28	203
2	0.20	0.54	0.44	129
3	0.20	0.80	0.65	87
4	0.20	1.08	0.88	65
5	0.30	0.28	0.15	434
6	0.30	0.50	0.27	241
7	0.30	0.79	0.43	151
8	0.30	1.09	0.59	110
9	0.30	1.53	0.83	78
10	0.40	0.25	0.10	1044
11	0.40	0.56	0.23	454
12	0.40	1.03	0.42	248
13	0.40	1.15	0.47	222
14	0.40	2.04	0.83	126
15	0.50	0.18	0.06	–
16	0.50	1.32	0.43	–
17	0.50	2.12	0.69	–

TABLE 1. Summary of experimental runs. The experimental variables together with the resolution with which they were determined: the initial angle of tilt θ ($\pm 0.03°$), the interface depth h_1 (± 0.2 cm) and the density difference between the upper and lower layers $\Delta\rho \approx 20$ kg m^{-3} (± 2 kg m^{-3}).

is not necessarily the result of supercritical flow conditions (see figure 1 with $h_1/H = 0.3$ and $\eta_o/h_1 = 0.9$), but is usually due to nonlinear steepening of a finite-amplitude wave. The evolution of the progressive surge is further discussed in §4.2.

In figure 5(a–e) interface displacement time series observed at wavegauge C (defined in figure 3) are compared to the linear analytical solution (2.9). The angle of tilt increases with each successive panel. For small W^{-1} (figure 5a), the interface is observed to oscillate about the equilibrium position in the same manner as predicted analytically, although viscous effects cause a continual decrease of amplitude with time. For large W^{-1} (figure 5c–e), a secondary wave (denoted by $\triangledown$) is observed approximately 30 s out of phase with the H1 seiche (denoted by $\blacktriangledown$). This wave is progressive in nature and is described below. As W^{-1} increases, dispersive, viscous and nonlinear processes cause the observed time series to deviate strongly from the analytical linear theory solution over shorter time scales. Solitary waves are observed at approximately T_s and viscous decay is evident through the decrease in observed wave amplitude over time. Spectral analysis of the time series at wave gauge C reveals the most energetic H1 mode as well as a series of odd modes consistent with the analytical model (figure 5f).

In figure 6(a–e), the interface displacement time series observed at wave gauge B are compared to the analytical solution. This wave gauge is located near the nodal position for the linear modes and therefore the analytical solution does not exhibit an interfacial displacement. For small W^{-1} (figure 6a), the system remains linear, matching the analytical solution. As W^{-1} is increased (figure 6b–e), an oscillation with period $T_i/2$ is observed. This oscillation must be a consequence of nonlinear effects and is progressive, passing the wave gauge twice during T_i (figure 4). For large W^{-1} (figure 6e) the progressive wave rapidly steepens into an internal surge which degenerates into solitary waves soon thereafter (as $t \rightarrow T_s$). Spectra of the interface displacement at wavegauge B (figure 6f) confirm the progressive surge signal to have the same $T_i/2$

FIGURE 4. Video frames showing the standing seiche, evolving progressive surge and solitary waves. The initial condition is shown in (*a*). The surge and solitary wave packet are propagating to the left in (*b*)–(*f*), reflecting off the endwall in (*g*) and to the right in (*h*)–(*i*). For this experiment $h_1/H = 0.3$, $\eta_o/h_1 = 0.9$, $T_i = 110$ s and $T_s = 40$ s.

frequency as the horizontal mode two (H2) mode with harmonics evident at other even modes. In both spectral plots (figures 5*f* and 6*f*) a bifurcation of the individual spectra is evident between approximately 5×10^{-2} Hz and 5×10^{-1} Hz indicating the frequency bandwidth containing the solitary waves.

The experimental observations reveal that the standing seiche, progressive surge and solitary waves occupy discrete bandwidths in frequency space. The discrete nature of the signals thus allows isolation of the component due to each wave group through selective filtering of the interface displacement time series in the frequency domain. In particular, the odd linear modes are recorded on wave gauges A and C, the even nonlinear modes on wave gauge B, and solitary waves on all wave gauges at frequencies below 5×10^{-2} Hz. The procedure for obtaining the temporal energy distribution in each of these modes is described below.

3.3. Decomposition of the internal wave field

The basin-scale H1 seiche signal was obtained by low-pass filtering the time series from the wave gauges located in non-nodal positions (wave gauges A and C) using a fourth-order Butterworth filter with a cutoff frequency located midway between the frequencies of the H1 and H2 modes (i.e. passes frequencies $f < (3/2)T_i$). This
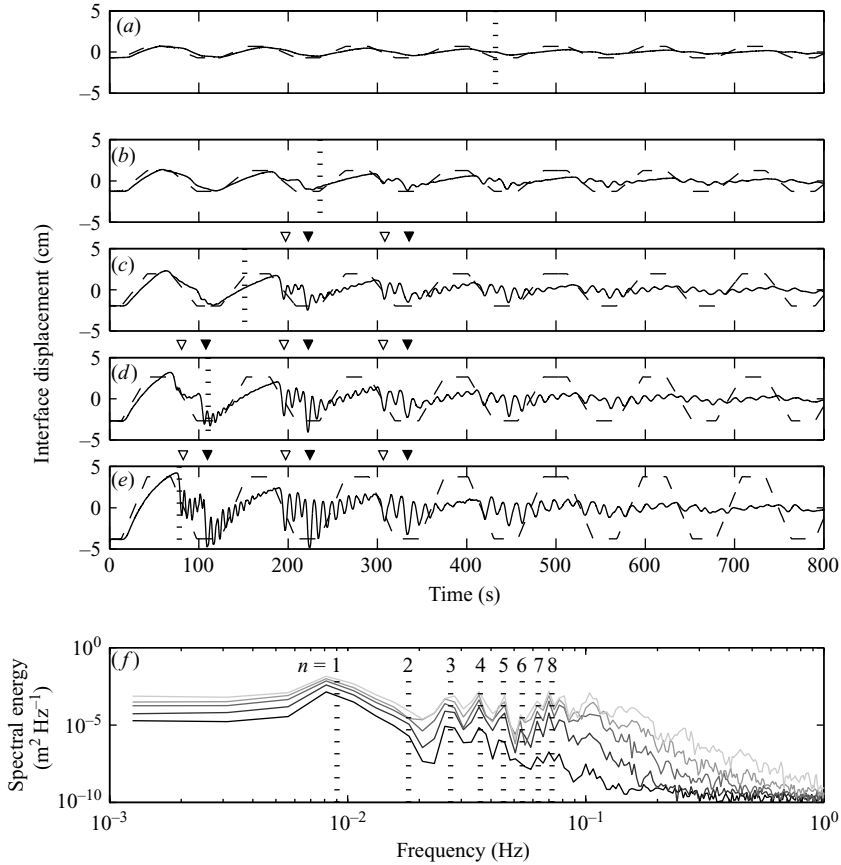
FIGURE 5. Time series of the observed interface displacement (solid line) and linear initial-value problem (broken line) at wave gauge C: (a) $\eta_o/h_1 = 0.15$; (b) $\eta_o/h_1 = 0.27$; (c) $\eta_o/h_1 = 0.43$; (d) $\eta_o/h_1 = 0.59$; (e) $\eta_o/h_1 = 0.83$. For the time series shown $h_1/H = 0.3$, $T_i = 109$ s and the vertical dotted lines denote T_s from equation (2.15). The ▼ and ▽ symbols denote crests of the observed H1 seiche and progressive surge, respectively. (f) Interface displacement spectra for the observed time series in (a) to (e). The bottom line corresponds to (a), etc. and the vertical dotted lines denote the frequencies of the lowest eight basin-scale standing modes calculated from (2.4).

bandwidth neglects the higher linear modes, which contain less that 1.5% of the basin-scale internal wave energy.

The signals associated with the progressive surge and solitary wave modes were observed at all three of the wave gauges. However, these signals were only filtered from the time series at wave gauge B, which as a nodal location is not contaminated by the motion of the H1 seiche. The surge and solitary wave signals were isolated using band-pass (surge) and high-pass (solitary waves) second-order Butterworth filters passing frequencies $(3/2)T_i < f < (1/3)T_i$ and $f > (1/3)T_i$, respectively. Figure 7(a–c) shows the filtered time series for a typical experiment where $W^{-1} = 0.44$ and $h_1/H = 0.2$. Note the occurrence of solitary waves at $t \approx T_s$ and the temporal decrease in amplitude of all the observed signals resulting from viscous effects. Comparison of figure 7(a) and figure 7(b), reveals the progressive surge to be of the same spatial form as the sinusoidal H1 seiche, yet increasing in amplitude as $t \to T_s$. The progressive nature of the surge results in a doubling of the wave frequency relative to the seiche.
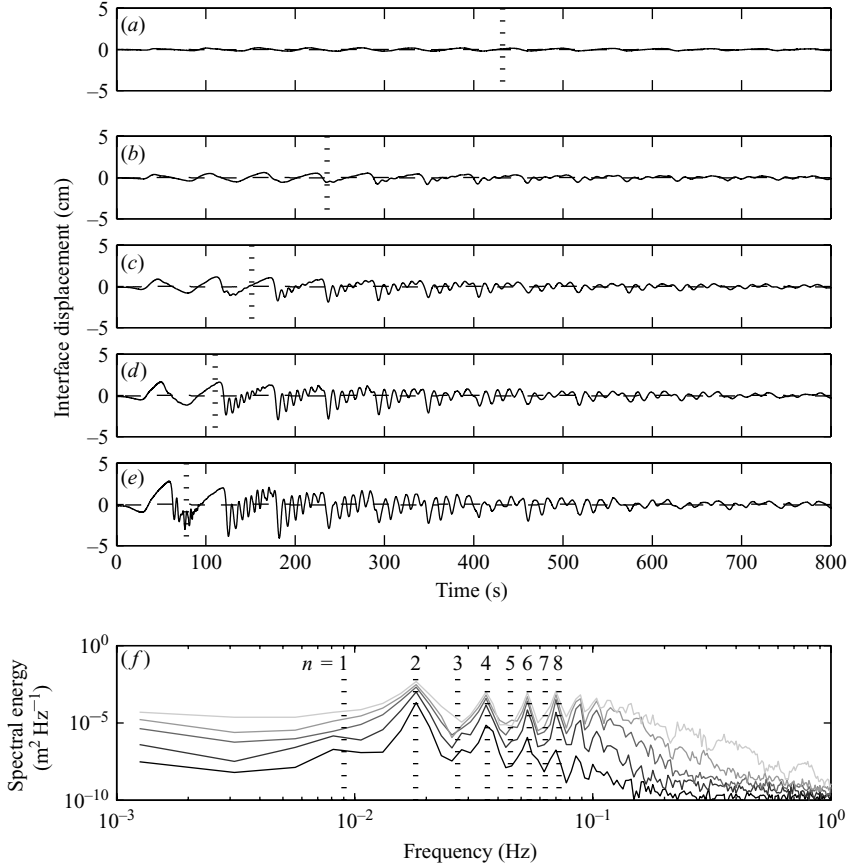
FIGURE 6. Same as figure 5 except at wave gauge B.

Assuming an equipartition between the kinetic and potential forms of wave energy (e.g. Bogucki & Garrett 1993), the total energy in each of the three filtered components was quantified in a particular wave period as twice the potential energy calculated using (2.7). To allow the integral to be evaluated directly from the filtered time series, the integrand was transformed from spatial to temporal coordinates using the linear phase speed (e.g. Michallet & Ivey 1999)

$$\text{Total energy} = c_o g \left(\rho_2 - \rho_1 \right) \int_{t_1}^{t_2} \eta^2(t) \, dt. \tag{3.1}$$

To apply (3.1) to the filtered standing seiche signal, it was first necessary to uncouple the left and right propagating components making up the standing-wave pattern. For these components, the assumption of an equipartition between kinetic and potential wave energy is valid. The total energy was then taken as the sum of the energy in the two components. The uncoupling was accomplished by first calculating the interface displacement $\eta(x, t)$ for all t over the tank length ($0 \leqslant x \leqslant L$), through a least-squares fit of a cosine function to the filtered interface displacements at wave gauges A, B and C. The maximum standing-wave amplitude was then evaluated at the endwall (i.e. $\eta(x = 0$ or $L, t)$). This amplitude was divided by two to give the equivalent amplitudes of the incident and reflected standing-wave components. The total energy was then individually calculated for each of these two components using
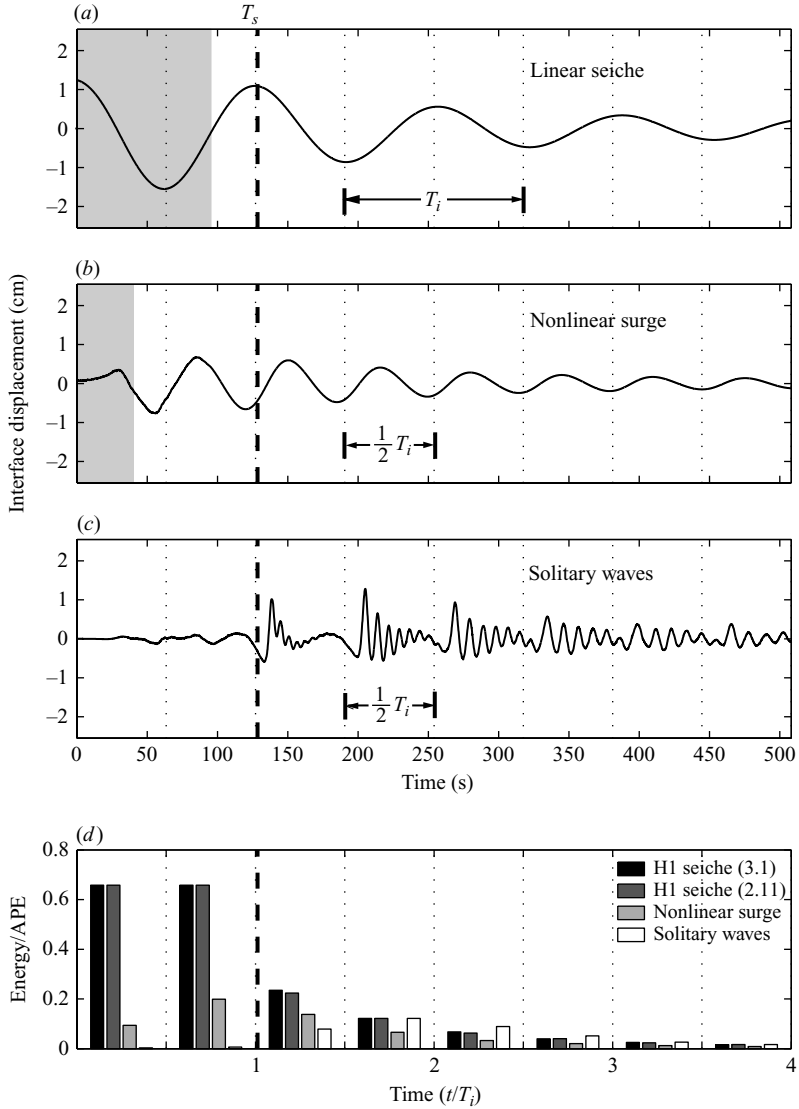
FIGURE 7. Filtered time series of the interface displacement for the experiment where $W^{-1} = 0.44$ and $h_1/H = 0.2$. (a) Linear-seiche from low-pass filter ($f < (3/2T_i)$) of wave gauge A signal, (b) progressive surge from band-pass filter ($(3/2T_i) < f < (1/3T_i)$) of wave gauge B signal, (c) solitary waves from high-pass filter ($f > (1/3T_i)$) of signal of wave gauge B signal. Shaded region denotes region where transient filter start-up effects were corrected. (d) Temporal evolution of the APE distribution between the wave groups in (a)–(c).

(3.1) and summed. For the progressive surge and solitary waves, $\eta(t)$ was simply the filtered time series. For all three wave groups, the integral in (3.1) was over $T_i/2$ as this is the time required for one wave/packet length to propagate through a particular wave gauge. Note that although the filtered time series are not orthogonal (i.e. $\eta = \eta_1 + \eta_2 + \eta_3$, but $(\eta_1 + \eta_2 + \eta_3)^2 \neq (\eta_1^2 + \eta_2^2 + \eta_3^2)$), the total wave energy evaluated from the unfiltered (raw) signal remains equal to the sum of the energy evaluated independently for the three filtered modes. This results from the filtered signals being solely a manifestation of the available potential energy in a particular mode, which are

subject to the equipartition required by (3.1). Conversely, the unfiltered signal exhibits modal interaction, which may favour the harbouring of energy in the kinetic form and does not necessitate that kinetic and potential energy remain equally partitioned (i.e. $C(\eta_1 + \eta_2 + \eta_3)^2 = 2(\eta_1^2 + \eta_2^2 + \eta_3^2)$, for $C \neq 2$).

To verify our methods, a second technique was applied to quantify the energy in the H1 seiche. The cosine function originally fitted to the interface displacements was integrated throughout the domain using (2.7). The total energy was obtained by evaluating the integral at times when the standing-wave crests and troughs were at the maximum amplitudes (i.e. $t = 0$, $T_i/2$, $T_i/4$, etc.) and all energy was in the potential form. Integrals evaluated at consecutive time intervals (e.g. $t = 0$ and $T_i/2$) were averaged to give a mean energy during that period. This allows for direct comparison with the results from (3.1).

To minimize start-up transients, several filter lengths of a reflected copy of the input signal were appended to the beginning of the time series. However, transients will still occur over $t < 1/f_h$, where f_h is the Nyquist or highest cutoff frequency (shown as a shaded region in figure 7a–c). To compensate for filter start-up with the linear seiche (figure 7a), the energy during the first period was taken as the average of the energy in the initial condition, from (2.8), and the H1 energy at $t = T_i$ using (3.1). Start-up was corrected for in figure 7(b) by replacing the filtered signal with the unfiltered signal within the shaded region. This simple substitution was permissible prior to the evolution of solitary waves at $t = T_s$. In figure 7(c) a correction for filter start-up was not required as both the filtered and unfiltered signals are near zero prior to the evolution of the solitary waves.

The results of these methods for determining the energy in the various wave groups are shown in figure 7(d) for a typical experimental run. The energy during each integral is normalized by the energy in the initial condition (APE) as determined from the observed displacements at $t = 0$ using (2.7). Both energy estimates for the H1 mode compare well, showing an exponential decrease in energy over time from around 65 % of APE during the first period to less than 5 % after four periods. Surprisingly, 10 % of APE is already observed in the progressive surge for time $t < T_i/2$. This energy increases to approximately 20 % as the surge steepens ($t \to T_s$), decreasing thereafter as the solitary wave packet attains its maximum energy at $t \approx 2T_i$.

3.4. *Experimental results*

The methods to partition the internal wave energy between the linear seiche, progressive surge and internal solitary waves were applied to the data from all experimental runs. The results are presented in figure 8, where in each panel the vertical axis is W^{-1} and the horizontal axis h_1/H are analogous to those presented in figure 1. In the figure matrix, the three columns represent the three wave groups, the rows show the evolution in time, and the contours in each plot denote the modal energy as a percentage of the observed APE at $t = 0$.

During $0 < t < T_i$ (figure 8a, e, i) for large h_1/H and small η_o/h_1, at least 50–70 % of the APE is accounted for by the standing H1 seiche, with less than 10% in the surge or solitary waves. For small h_1/H and large η_o/h_1, 20–60 %, 0–20 % and 0–10 % of the APE is in the seiche, surge and solitary waves, respectively. The energy content in the H1 seiche thus increases as the system becomes 'linear' (i.e. $\eta_o/h_1 \to 0$ and $h_1/H \to 0.5$) and decreases uniformly throughout the domain with time (figure 8a–d). The partition of energy in the progressive surge (figure 8e–h) is greater when the system is 'nonlinear' (i.e. $\eta_o/h_1 \to 1$ and $h_1/H \to 0$), thus accounting for the reversed energy gradient relative to that of the H1 seiche. Nonlinear steepening initially occurs
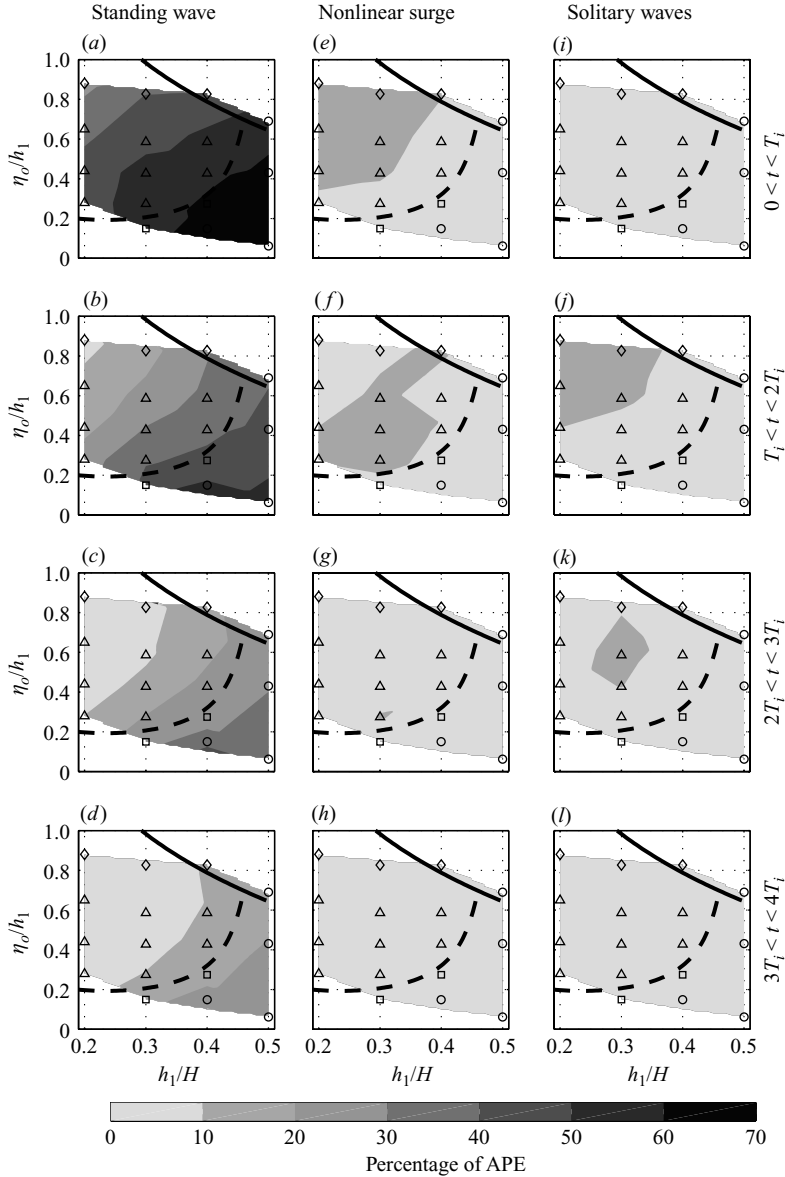
FIGURE 8. Temporal evolution of APE distribution between the component internal wave modes. The axes and regime boundaries of each panel are as in figure 1.

over $0 < t < T_i$ in the 'more nonlinear' region of the domain (figure 8*e*). For these experiments $T_i < T_s < 2T_i$, causing an observed energy flux to the solitary wave mode, (*e*)–(*j*), rather than energy being conserved in the surge with time, (*e*)–(*j*). In the 'less nonlinear' region, nonlinear and dispersive effects occur over longer time scales $T_i < t < 2T_i$ and $2T_i < t < 3T_i$, respectively, yet the energy flux to the sub-basin-scale solitary mode is maintained (the energy flows from (*f*) to (*k*), rather than (*f*) to (*g*)). Note that there is little observed energy loss during this dispersive energy transfer from low to high-frequency. These results do not account for the energy loss by the action of viscosity, which eventually damps all motions. Quantification of this loss is

Mode	Equation	Source
H1 seiche	$\dfrac{\mathrm{d}E_{H1}}{E_{H1}} \sim \dfrac{\pi\delta_b A_b}{V} + \dfrac{\nu H T_i}{\delta_\rho h_1 h_2}$	Horn *et al.* (2001)
Nonlinear surge	$\dfrac{\mathrm{d}E_{NS}}{E_{NS}} \sim (1 - e^{-\sigma L})$	Troy (2003)
Solitary waves	$\dfrac{\mathrm{d}E_{SW}}{\mathrm{d}t} \sim \dfrac{4\sqrt{2}\rho_2(1 - \rho_1/\rho_2)g^{5/4}\nu^{1/2}\,\lvert\bar{\eta}\rvert^{7/4}}{3^{1/4}\pi^{3/2}\left(h_1 h_2^2\,\lvert h_1^2 - h_2^2\rvert\right)^{1/4}}$ $\times \left[\left(1 + \dfrac{2h_2}{B}\right)h_1^2 + \dfrac{2h_1 h_2^2}{B} + \tfrac{1}{2}(h_1 + h_2)^2\right]$	Leone *et al.* (1982)

TABLE 2. Viscous damping equations. A_b is the total boundary area, V is the tank volume, ν is the kinematic viscosity and δ_ρ is the thickness of the density interface (taken as 1 cm), $\delta_b \approx (\nu T_i/\pi)^{1/2}$ is the thickness of the oscillatory boundary layer (Batchelor 1967, pp. 193 and 354). σ is the sum of the individual decay rates resulting, in order of dominance, from: sidewall boundary-layer dissipation, interfacial dissipation, bottom boundary-layer dissipation and internal dissipation (see Troy (2003) for the decay rate equations). B is the channel width and $\bar{\eta}(t)$ is the maximum solitary-wave amplitude (taken as the maximum amplitude in each solitary wave packet). See text for description of other symbols.

required to close the energy budget and so it is theoretically estimated in the following section.

4. Discussion

4.1. *Estimation of viscous damping*

We have quantified the energy in each of the three component internal wave modes: the basin-scale standing seiche, the progressive surge and the solitary waves. Wave breaking was not observed, which implies that the majority of wave energy is ultimately lost by the action of viscosity. Assuming laminar boundary and interfacial layers, this viscous loss was theoretically estimated for each of the wave modes in isolation.

The fraction of wave energy dissipated from the standing H1 wave during one internal wave period $\mathrm{d}E_{H1}/E_{H1}$ was estimated for the laboratory experiments considering both the losses at the solid boundaries and in the interfacial shear layer. Horn *et al.* (2001) integrated these losses for one wave period over the solid boundaries in each layer (excluding endwalls) and the interfacial area table 2. The first term is the energy loss at the solid boundaries and the second term the loss in the interfacial shear layer. The fraction of progressive surge energy which is lost to viscous damping during one wave period $\mathrm{d}E_{NS}/E_{NS}$ was estimated using a theoretical model by Troy (2003). In this formulation the total energy equation is integrated vertically and laterally for progressive interfacial waves in a laterally bounded rectangular channel table 2. Finally, the rate of energy loss from the solitary waves $\mathrm{d}E_{SW}/\mathrm{d}t$ was estimated, for a KdV type interfacial solitary wave propagating in a rectangular channel, using the model by Leone, Segur & Hammack (1982) (table 2). Of the three terms on the right-hand side of this expression, the first and second represent the energy loss from the lower and upper fluid layers along the rigid boundaries, respectively, and the third term represents the energy loss at the interface. The total energy loss was quantified by summing the loss from each of these three components. This loss was applied to close the energy budget.
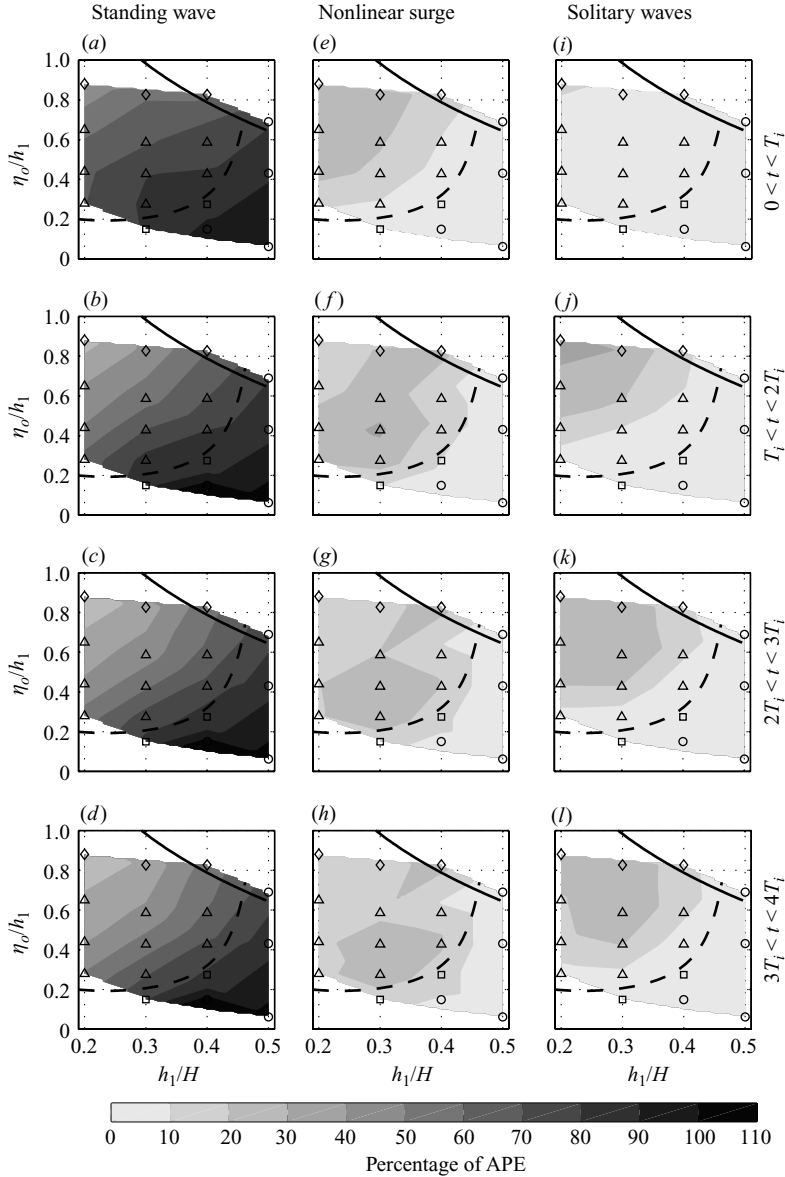
FIGURE 9. Same as figure 8, but viscous energy losses are accumulated
with time along each column.

In figure 9, the axes, columns and rows are analogous to figure 8; however, the contours at each time interval denote the sum of both the observed wave energy and the cumulative theoretical viscous loss. Again, the energy is presented as a percentage of the observed APE. Comparison to figure 8 reveals that 20 %, 10 % and 10 % of the energy from the seiche, surge and solitary waves, respectively, may be dissipated owing to viscosity in the first period alone. Most strikingly, panels (c)–(d), (g)–(h) and (k)–(l) are nearly identical. Therefore, there is little or no energy flux between modes for $t > 2T_i$; an indication that after the initial nonlinear distribution of energy between the H1 seiche and surge and the subsequent dispersive energy flux to the solitary waves, the internal modes remain uncoupled.

4.2. *The progressive surge and solitary waves*

An essential feature of the downscale energy flux linking the initial basin-scale motions to the higher-frequency solitary waves is the progressive surge. The amount of energy in the surge is a function of the degree of nonlinearity of the system. This may be expressed as a single non-dimensional parameter (rather than W^{-1} and h_1/H) taken as the ratio of the linear and nonlinear terms in (2.16)

$$\frac{\alpha \eta_o}{c_o} \equiv \frac{3\eta_o}{2} \frac{|h_1 - h_2|}{h_1 h_2}, \tag{4.1}$$

where we have taken $\eta \sim \eta_o \sim a$. In this formulation, nonlinearities are incorporated owing to both increasing W^{-1} and decreasing h_1/H. A value of $\alpha a/c_o \sim 0.1$ has been shown to be sufficient for visible nonlinear wave deformation (Holloway & Pelinovsky 2001, p. 42). In figure 10(*a*), the normalized energy in the surge E_{NS}/APE is plotted versus $\alpha \eta_o/c_o$. Averaged over each wave period, the data collapse to a single line, which has been obtained as a least-squares fit (see figure caption for details). For $\alpha \eta_o/c_o > 0.4$, the surge is excited during the first period and the system is sufficiently nonlinear that the maximum energy fraction

$$\frac{E_{NS}}{\mathrm{APE}} \approx 0.2. \tag{4.2}$$

For $0 < \alpha \eta_o/c_o < 0.4$, the maximum surge energy is obtained during the second period, because here $2T_i > T_s > T_i$. In general, the maximum energy increases in direct proportion to $\alpha \eta_o/c_o$ and is given by

$$\frac{E_{NS}}{\mathrm{APE}} \approx 0.5 \frac{\alpha \eta_o}{c_o}. \tag{4.3}$$

For $t > 2T_i$, there is no further energy flux between modes, and the surge energy decreases uniformly owing to the action of viscosity (in agreement with figure 9).

In figure 10(*b*), E_{NS}/APE contours drawn from the least-squares data in figure 10(*a*) are presented in the $(\alpha \eta_o/c_o) - T_i$ plane. Also plotted on figure 10(*b*) is the curve of T_s versus $\alpha \eta_o/c_o$, showing the T_s data to collapse to a single line, which is coincident with the ridge of maximum surge energy. The energy in the progressive surge is shown to have increased during an initial nonlinear steepening phase $(0 < t \leqslant T_s)$ and retained up to 20 % of the APE at $t \approx T_s$. For $t > T_s$, the E_{NS}/APE decreased from this maximum, with a corresponding increase in ISW energy, until eventually all of the surge energy was transferred to the solitary waves with little loss (figure 10*c*). In the absence of sloping topography, the energy in the ISW packet was ultimately lost to viscosity on time scales of order $3T_i$ to $5T_i$. These results are consistent with analytical models (2.15) which shows that the surge steepens as $t \to T_s$ and subsequently degenerates into solitary waves. Why the energy in the progressive surge is limited to 20 % of APE remains unknown.

We may investigate the evolution of the progressive surge from the initial condition by conceptualizing the wave field as being composed of two separate parts, both emanating from the positive and negative displacement volumes that initially co-exist, but are spatially separated. If we consider displacements of very small amplitude, such as those governed by linearized equations, there is no qualitative distinction between the resulting left and right propagating waves. These components form the standing seiche. However, for larger displacements the negative initial volume will evolve into a packet of solitary waves of depression, while the positive initial volume evolves into a positive dispersive wave, referred to as a rarefaction (Horn *et al.* 2002). The lack of symmetry between the two finite-amplitude components is a direct consequence of the
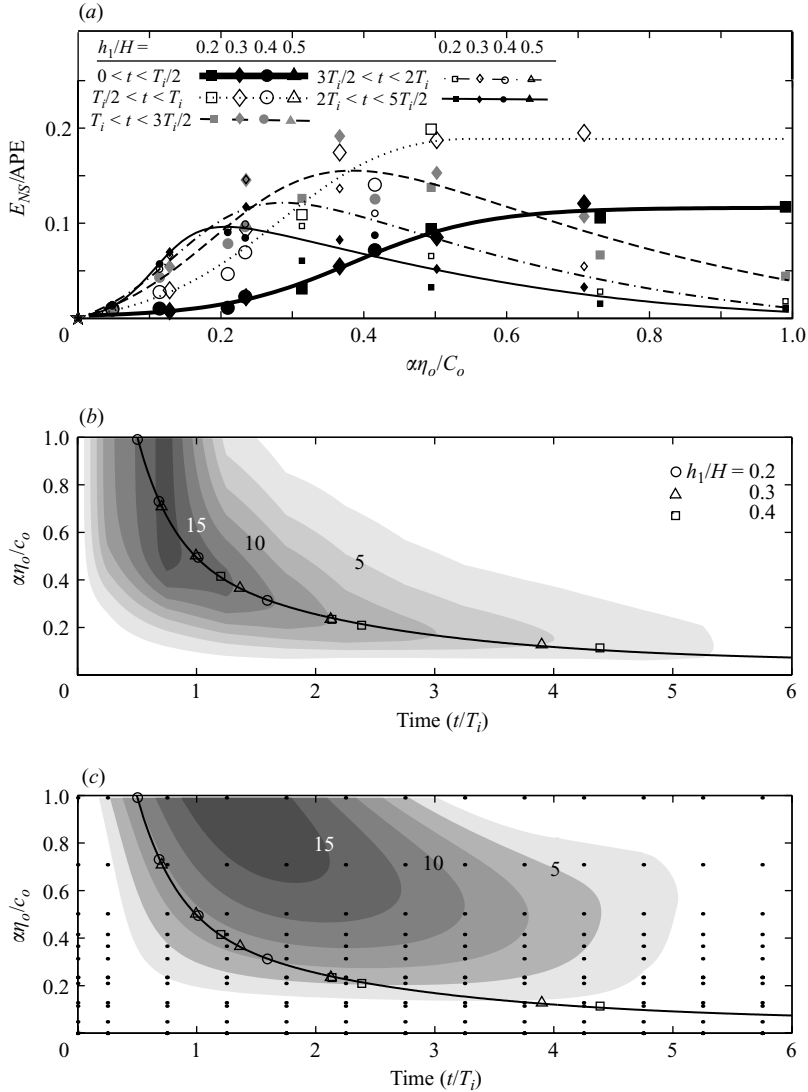
FIGURE 10. (*a*) Relationship between the fraction of APE observed as energy in the progressive surge E_{NS}, and the nonlinearity of the system $\alpha\eta_o/c_o$ over each of the first five T_i. Squares, diamonds, circles and triangles represent $h_1/H = 0.2$, 0.3, 0.4 and 0.5, respectively. All curves are nonlinear least-squares fit. (*b*) Evolution of $E_{NS}/$APE in the ($\alpha\eta_o/c_o$, T_i)-plane from (*a*). (*c*) Evolution of $E_{ISW}/$APE in the ($\alpha\eta_o$, c_oT_i)-plane. Contours are least-squares fit to the data points (indicated by ·). In (*a*) and (*b*) the contours are presented as a percentage of the APE introduced at $t=0$ with a contour interval of 2.5 %. The solid line denotes T_s fitted to pass through values at $h_1/H = 0.2$, 0.3, 0.4 and 0.5.

nonlinearity of the governing equations (e.g. Stoker 1957, p. 306) and the progressive nature of the internal surge and solitary wave packet results from the combination of these asymmetrical modes.

4.3. *Field observations*

To determine the applicability of our analysis to real lakes, we computed the temporal evolution of the modal energy content for a lake with suitable field data (Baldeggersee,
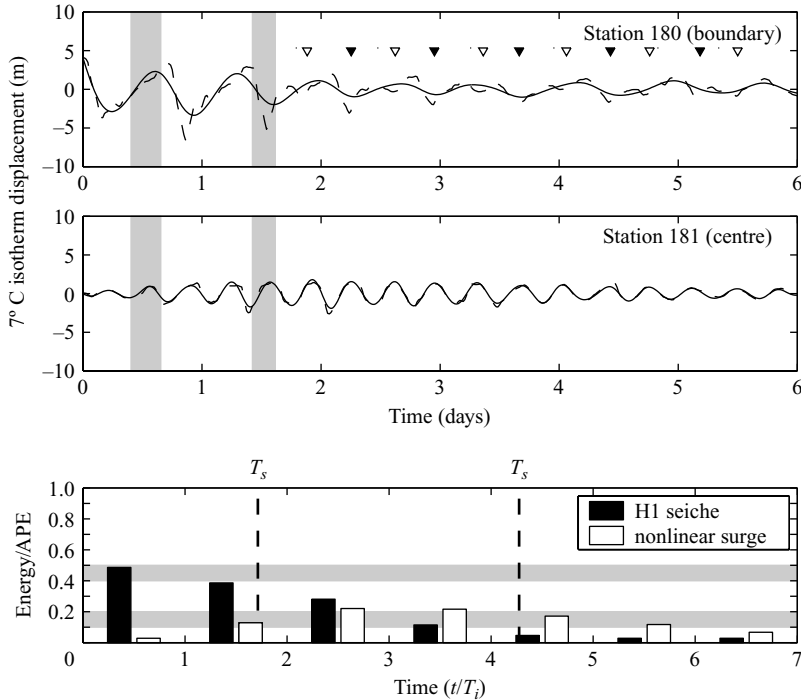
FIGURE 11. Raw (——) and filtered (—) time series of the 7° isotherm displacement from Baldeggersee at (*a*) station 180 and (*b*) station 181. The time series are filtered as described in §3.3. The lake was subject to three along axis wind events. The first wind event ceases at the origin of the time axis, while the timing of the second and third events is denoted by vertical shading. The initial energy APE was evaluated as the maximum isotherm displacement, extrapolated to the lake perimeter, during the forcing events. The ▼ and ▽ symbols denote crests of the H1 seiche and progressive surge, respectively. (*c*) Temporal evolution of the APE distribution between the H1 seiche and progressive surge. Horizontal shading denotes the expected energy distributions as given by figure 8(*a*, *e*). For this data $h_1 = 10$ m (Lemmin 1987), $H = 34$ m (Imboden *et al.* 1983), $\eta_o \approx 5$ m, $W^{-1} = 0.4$, $h_1/H = 0.3$, $T_i \approx 16$ h and $T_s \approx 30$ h. Note that in (*c*), T_s (——) is presented from the end of both the first and third wind events.

Switzerland). This small deep lake with a rectangular basin shape is subject to pulses of high wind stress along the major axis. Published observations were digitally recovered during a period of seasonal stratification with three along axis wind events (Lemmin 1987, his figure 6). These observations occurred at stations positioned in a manner analogous to our distribution of wave gauges, being both near the centre of the lake and near the boundaries. To allow comparison with our two-layer experiments, the motion of the internal wave field initiated by the wind was isolated as the displacement of the 7° isotherm (located in the centre of the metalimnion), and filtered as described in §3.3.

Raw and filtered time series (figure 11*a*, *b*) are qualitatively consistent with the laboratory results (figure 8*a*, *b*), particularly the relative phase and amplitude of the H1 seiche and surge crests. The H1 seiche energy is initially between 40 % and 50 % of the APE and as $t \to T_s$ the energy content in the surge is maximal near 20 % of the APE (figure 11*c*). These results are in quantitative agreement with figures 8(*a*) and (*e*), respectively. Viscous damping appears to be weaker than experimentally observed, with the surge energy persisting at greater than the 10 % level for the first six periods,

although this may be a consequence of resonant wind forcing. Solitary wave packets were not observed, but such waves would be aliased by the 20 min sampling period. This period is much greater than the theoretical solitary wave period calculated from (2.18), with $a \sim \eta_o$, to be $T_{ISW} = \lambda/c \approx 43/0.14 \approx 300$ s. High-frequency internal solitary wave packets have been observed to occur in other lakes after strong wind forcing events (e.g. Thorpe, Hall & Crofts 1972; Hunkins & Fliegel 1973; Farmer 1978; Boegman *et al.* 2003). These waves are thought to result from nonlinear processes and may each possess $\sim 1\%$ of the energy within the basin-scale internal wave field. Furthermore, the wave packets are capable of propagating to the lake perimeter where they can shoal, thus releasing their energy directly to the benthic boundary layer.

The question remains as to what would occur if the solitary wave packet impinged upon sloping topography at the lake boundary. Results presented by Boegman, Ivey & Imberger (2005) and the work of Helfrich (1992) and Michallet & Ivey (1999) demonstrate that as much as 90–95% of the energy contained within the solitary wave packet may be lost in a single wave-sloping boundary interaction process, thus enhancing localized mixing and dissipation. Furthermore, if the system were periodically forced it may be imagined that a quasi-steady state is achieved, whereby up to 20% of APE is continually found in the surge and solitary wave modes. This energy would be conveyed to the lake boundary, the particular spatial and temporal energy distributions being governed by the topography and the relative frequencies $1/T_i$, $1/T_s$ and that of the forcing. We leave these outstanding issues to be addressed elsewhere.

5. Conclusions

We have extended the work of Thorpe (1971, 1974) and Horn *et al.* (2001) by quantifying the temporal distribution of energy between the three component internal wave modes. Our model is both qualitatively and quantitatively consistent with published field observations. Depending upon the initial conditions, during $0 < t < T_i$ between 20% and 70% of the APE may be found in the H1 seiche, with less than 20% and 10% in the surge and solitary waves, respectively. The remainder is lost to the action of viscosity. These findings demonstrate that linear analytical models may significantly underestimate the total energy contained in the internal wave field. Furthermore, such linear models cannot describe the development of the progressive surge, which serves as a vital link between basin-scale and sub-basin-scale motions. The surge receives up to 20% of the APE during the nonlinear steepening phase $(t < T_s)$ and, in turn, conveys all of this energy to the smaller-scale solitary waves as dispersion becomes significant $(t > T_s)$. This temporal energy flux may be quantified in terms of the ratio of the linear and nonlinear terms in the nonlinear non-dispersive wave equation. Through estimation of the viscous energy loss, it was established that all modal energy flux occurred while $t < 2T_i$, the modes being independently damped thereafter. Finally, it is evident that this degeneration process, which is both non-hydrostatic and sub-grid scale, remains as a challenge to be captured by field-scale hydrodynamic models.

REFERENCES

APEL, J. R., HOLBROOK, J. R., LIU, A. K. & TSAI, J. J. 1985 The Sulu Sea internal soliton experiment. *J. Phys. Oceanogr.* **15**, 1625–1650.

BATCHELOR, G. K. 1967 *An Introduction to Fluid Dynamics*. Cambridge University Press.

BENNEY, D. J. 1966 Long nonlinear waves in fluid flows. *J. Maths Phys.* **45**, 52–63.

BOEGMAN, L., IMBERGER, J., IVEY, G. N. & ANTENUCCI, J. P. 2003 High-frequency internal waves in large stratified lakes. *Limnol. Oceanogr.* **48**, 895–919.

BOEGMAN, L., IVEY, G. N. & IMBERGER, J. 2005 The degeneration of internal waves in lakes with sloping topography. *Limnol. Oceanogr.* (accepted, subject to revision).

BOEGMAN, L., LOEWEN, M. R., HAMBLIN, P. F. & CULVER, D. A. 2001 Application of a two-dimensional hydrodynamic reservoir model to Lake Erie. *Can. J. Fish. Aquat. Sci.* **58**, 859–869.

BOGUCKI, D. & GARRETT, C. 1993 A simple model for the shear-induced decay of an internal solitary wave. *J. Phys. Oceanogr.* **23**, 1767–1776.

CUSHMAN-ROISIN, B. 1994 *Introduction to Geophysical Fluid Dynamics*. Prentice–Hall.

DJORDJEVIC, V. & REDEKOPP, L. G. 1978 The fission and disintegration of internal solitary waves moving over two-dimensional topography. *J. Phys. Oceanogr.* **8**, 1016–1024.

DRAZIN, P. G. & JOHNSON, R. S. 1989 *Solitons: an Introduction*. Cambridge University Press.

FARMER, D. M. 1978 Observations of long nonlinear internal waves in a lake. *J. Phys. Oceanogr.* **8**, 63–73.

FISCHER, H. B., LIST, E. J., KOH, R. C. Y., IMBERGER, J. & BROOKS, N. H. 1979 *Mixing in Inland and Coastal Waters*. Academic.

GEAR, J. A. & GRIMSHAW, R. 1983 A second-order theory for solitary waves in shallow fluids. *Phys. Fluids* **26**, 14–29.

GILL, A. E. 1982 *Atmosphere–Ocean Dynamics*. Academic.

HAMMACK, J. L. & SEGUR, H. 1978 Modelling criteria for long water waves. *J. Fluid Mech.* **84**, 359–373.

HEAPS, N. S. & RAMSBOTTOM, A. E. 1966 Wind effects on the water in a narrow two-layered lake. *Phil. Trans. R. Soc. Lond.* A **259**, 391–430.

HELFRICH, K. R. 1992 Internal solitary wave breaking and run-up on a uniform slope. *J. Fluid Mech.* **243**, 133–154.

HENDERSON, F. M. 1966 *Open Channel Flow*. Macmillan.

HODGES, B. R., IMBERGER, J., LAVAL, B. & APPT, J. 2000 Modeling the hydrodynamics of stratified lakes. In *Proc. Hydroinformatics Conf.* Iowa Institute of Hydraulic Research.

HOLLOWAY, P. & PELINOVSKY, E. 2001 Internal tide transformations and oceanic internal solitary waves. In *Environmental Stratified flows* (ed. R. Grimshaw), pp. 29–60. Kluwer.

HORN, D. A., IMBERGER, J. & IVEY, G. N. 1999 Internal solitary waves in lakes – a closure problem for hydrostatic models. In *11th Aha Huliko Hawaiian Winter Workshop – Internal Gravity Waves II*. University of Hawaii.

HORN, D. A., IMBERGER, J. & IVEY, G. N. 2001 The degeneration of large-scale interfacial gravity waves in lakes. *J. Fluid Mech.* **434**, 181–207.

HORN, D. A., IMBERGER, J., IVEY, G. N. & REDEKOPP, L. G. 2002 A weakly nonlinear model of long internal waves in closed basins. *J. Fluid Mech.* **467**, 269–287.

HUNKINS, K. & FLIEGEL, M. 1973 Internal undular surges in Seneca Lake: a natural occurrence of solitons. *J. Geophys. Res.* **78**, 539–548.

IMBERGER, J. 1998 Flux paths in a stratified lake: a review. In *Physical Processes in Lakes and oceans* (ed. J. Imberger), *Coastal and Estaurine Studies*, vol. 54, pp. 1–18. AGU.

IMBODEN, D. M., LEMMIN, U., JOLLER, T. & SCHURTER, M. 1983 Mixing processes in lakes: mechanisims and ecological relevance. *Schweiz. Z. Hydrol.* **45**, 11–44.

KAKUTANI, T. & YAMASAKI, N. 1978 Solitary waves on a two-layer fluid. *J. Phys. Soc. Japan* **45**, 674–679.

KUNZE, E., ROSENFELD, L. K., CARTER, G. S. & GREGG, M. C. 2002 Internal waves in Monterey Submarine Canyon. *J. Phys. Oceanogr.* **32**, 1890–1913.

LANDAU, L. D. & LIFSHITZ, E. M. 1959 *Quantum Mechanics – Non-relativistic Theory*. Pergamon.

LEMMIN, U. 1987 The structure and dynamics of internal waves in Baldeggersee. *Limnol. Oceanogr.* **32**, 43–61.

LEONE, C., SEGUR, H. & HAMMACK, J. L. 1982 Viscous decay of long internal solitary waves. *Phys. Fluids* **25**, 942–944.

LONG, R. R. 1972 The steepening of long internal waves. *Tellus* **24**, 88–99.

MACINTYRE, S., FLYNN, K. M., JELLISON, R. & ROMERO, J. R. 1999 Boundary mixing and nutrient fluxes in Mono Lake, California. *Limnol. Oceanogr.* **4**, 512–529.

MICHALLET, H. & BARTHÉLEMY, E. 1997 Ultrasonic probes and data processing to study interfacial solitary waves. *Exps. Fluids* **22**, 380–386.

MICHALLET, H. & IVEY, G. N. 1999 Experiments on mixing due to internal solitary waves breaking on uniform slopes. *J. Geophys. Res.* **104**, 13 467–13 477.

MILLER, P. D. & CLARKE, S. R. 2001 An exactly solvable model for the interaction of linear waves with Korteweg–de Vries solitons. *SIAM J. Math. Anal.* **33**, 261–285.

MORTIMER, C. H. 1955 Some effects of the Earth's rotation on water movement in stratified lakes. *Proc. Intl Assoc. Appl. Limnol.* **12**, 66–77.

MORTIMER, C. H. 1974 Lake hydrodynamics. *Mitt. Internat. Verein. Limnol.* **20**, 124–197.

MORTIMER, C. H. & HORN, W. 1982 Internal wave dynamics and their implications for plankton biology in the Lake of Zurich. *Mitt. Internat. Verein. Limnol.* **127**, 299–318.

NEW, A. L. & PINGREE, R. D. 2000 An intercomparison of internal solitary waves in the Bay of Biscay and resulting from Korteweg–de Vries-type theory. *Prog. Oceanogr.* **45**, 1–38.

OSTROVSKY, I., YACOBI, Y. Z., WALLINE, P. & KALIKHMAN, I. 1996 Seiche-induced mixing: its impact on lake productivity. *Limnol. Oceanogr.* **4**, 323–332.

PEREGRINE, D. H. 1966 Calculations of the development of an undular bore. *J. Fluid Mech.* **25**, 321–330.

REDEKOPP, L. G. 2000 Boussinesq theory for internal wave evolution in a confined basin. In *Proc. Fifth International Symp. on Stratified Flow*. Vancouver, British Columbia.

SPIGEL, R. H. & IMBERGER, J. 1980 The classification of mixed-layer dynamics in lakes of small to medium size. *J. Phys. Oceanogr.* **10**, 1104–1121.

STOKER, J. J. 1957 *Water Waves*. Interscience.

THOMPSON, R. O. R. Y. & IMBERGER, J. 1980 Response of a numerical model of a stratified lake to wind stress. In *Second Intl Symp. Stratified Flows* (ed. T. Carstens & T. McClimans), pp. 562–570. Trondheim, Norway.

THORPE, S. A. 1971 Asymmetry of the internal seiche in Loch Ness. *Nature* **231**, 306–308.

THORPE, S. A. 1974 Near-resonant forcing in a shallow two-layer fluid: a model for the internal surge in Loch Ness? *J. Fluid Mech.* **63**, 509–527.

THORPE, S. A., HALL, A. & CROFTS, I. 1972 The internal surge in Loch Ness. *Nature* **237**, 96–98.

TROY, C. D. 2003 The breaking and mixing of progressive internal waves. PhD thesis, Department of Civil and Environmental Engineering, Stanford University.

WATSON, E. R. 1904 Movements of the waters of Loch Ness, as indicated by temperature observations. *Geog. J.* **24**, 430–437.

WEDDERBURN, E. M. 1907 Temperature of the fresh-water lochs of scotland. *Trans. R. Soc. Edin.* **45**, 407–489.

WHITHAM, G. B. 1974 *Linear and Nonlinear Waves*. Wiley.